

18 **Abstract**

19 A foundational assumption in paleomagnetism is that the Earth’s magnetic field
 20 behaves as a geocentric axial dipole (GAD) when averaged over sufficient timescales. Com-
 21 pilations of directional data averaged over the past 5 Ma yield a distribution largely com-
 22 patible with GAD, but the distribution of paleointensity data over this timescale is in-
 23 compatible. Reasons for the failure of GAD include: 1) Arbitrary “selection criteria” to
 24 eliminate “unreliable” data vary between studies, so the paleointensity database may in-
 25 clude biased results. 2) The age distribution of existing paleointensity data varies from
 26 latitude to latitude so different latitudinal averages likely represent different time peri-
 27 ods. 3) The time-averaged field could be truly non-dipolar. Here, we present a consis-
 28 tent methodology for analyzing paleointensity results and comparing time-averaged pa-
 29 leointensities from different studies. We apply it to data from Plio/Pleistocene Hawai’ian
 30 igneous rocks, sampled from fine-grained, quickly cooled material (lava flow tops, dike
 31 margins and scoria cones) and subjected to the IZZI-Thellier technique; the data were
 32 analyzed using the BiCEP method of Cych et al (2021, doi:10.1029/2021GC009755), which
 33 produces accurate paleointensity estimates without arbitrarily excluding specimens from
 34 the analysis. We constructed a paleointensity curve for Hawai’i over the Plio/Pleistocene
 35 using the method of Livermore et al (2018, doi:10.1093/gji/ggy383), which accounts for
 36 age distribution and has robust uncertainties. We demonstrate that even with the large
 37 uncertainties associated with obtaining a mean field from temporally sparse data, our
 38 average paleointensities obtained from Hawai’i and Antarctica (from Asefaw et al., 2021,
 39 doi:10.1029/2020JB020834, reanalyzed here) are not GAD-like after about 1.5 Ma.

40 **Plain Language Summary**

41 Paleomagnetists make the assumption that the Earth’s magnetic field behaves like
 42 a bar magnet centered at the spin axis, known as a Geocentric Axial dipole or GAD. Com-
 43 pilations of the magnetic field’s direction are consistent with this assumption, but com-
 44 pilations of its strength (paleointensity) are not. A number of causes for this could be:
 45 1) The different experimental methods and the criteria used to pass or exclude paleoin-
 46 tensity data might cause differences in records. 2) The ages of records differ between lo-
 47 cations. 3) The field really doesn’t behave like a bar magnet. To test this, we performed
 48 paleointensity experiments on rocks collected in Hawai’i and compared our results to re-
 49 sults of similar age from other locations analyzed using the same methodology. The three
 50 locations analyzed in this study do not produce time-averaged paleointensities consis-
 51 tent with a GAD field for the most recent 1.5 million years, but a GAD field cannot be
 52 ruled out before this time. This indicates that differences in time-averaged field strength
 53 in global records can be unrelated to differences in methodology or age between stud-
 54 ies.

55 **1 Introduction**

56 Paleomagnetists use the direction of the magnetization acquired in the Earth’s an-
 57 cient magnetic field to obtain estimates of the ancient latitude at which the rock formed.
 58 Calculation of a latitude relies on an assumption that the Earth’s magnetic field is struc-
 59 tured like a bar magnet when averaged over sufficiently long timescales, so that the mag-
 60 netic field is vertical at the poles, and horizontal at the equator, also termed a Geocen-
 61 tric Axial Dipole (GAD). Estimates of the Earth’s magnetic field direction, taken from
 62 different latitudes over the past 10 Ma conform relatively well to a GAD field, with a
 63 small hemispheric asymmetry (Cromwell et al., 2018). On the other hand, estimates of
 64 the Earth’s magnetic field strength (the paleointensity) averaged over the last 5 Ma con-
 65 sistently show a behaviour incompatible with a strongly dipolar field. A seemingly per-
 66 sistent feature in paleointensity data is the presence of weak paleofields at high south-
 67 ern latitudes (Lawrence et al., 2009; Asefaw et al., 2021; Tauxe et al., 2022), which causes

68 a hemispheric asymmetry in the paleointensity data. This is seen in paleointensities from
 69 the MagIC database over the last 5 Ma (plotted in Figure 1a) where the mean paleoin-
 70 tensity at 80°S would be produced by a centered magnetic dipole with a moment of around
 71 40 ZAm², whereas the mean paleointensity at 20°N would require a dipole moment with
 72 a magnitude closer to 80 ZAm². Attempts to fit Giant Gaussian Process (GGP) mod-
 73 els to paleointensity data to determine the structure of the time-averaged field have found
 74 that the field consistently requires a strong quadrupole term 15-30% the strength of the
 75 dipole field (Muxworthy, 2017; Shcherbakov et al., 2019), producing this asymmetry. How-
 76 ever, such a large quadrupole is completely incompatible with the directional data.

77 Three different hypotheses could explain the non-dipole like behaviour of global time-
 78 averaged paleointensity records: bias in paleointensity estimation, comparison of tem-
 79 porally distinct data in a time varying field, and genuine non-dipole field behavior. Re-
 80 garding the issue of bias, paleointensity estimation involves normalizing the observed nat-
 81 ural remanent magnetization (NRM) to a magnetization acquired in a known laboratory
 82 field. The accurate determination of a paleointensity therefore requires that the acqui-
 83 sition of a magnetization be reproducible in the laboratory. However, it has been shown
 84 (e.g., Levi, 1977; Dunlop & Özdemir, 2001; Krása et al., 2003; Tauxe et al., 2021) that
 85 some rocks have non reproducible magnetizations, which can lead to biased paleointen-
 86 sity estimates. Global paleointensity records may be confounded by these biased esti-
 87 mates, leading to an apparent non dipole signature. Alternatively, geomagnetic intensi-
 88 ty variations through time may not be well averaged. The majority of paleointensity
 89 determinations are made with volcanic rocks, which record an instantaneous snapshot
 90 of the magnetic field at the time they cool. Archeomagnetic data indicate that the Earth’s
 91 magnetic field strength can vary strongly over decades to centuries (e.g., Shaar et al.,
 92 2020), so numerous paleointensity estimates are necessary for a good average. If the field
 93 strength varies over long timescales (e.g., millions of years), then comparing the “aver-
 94 age” of two studies may not be meaningful if the units sampled are of different ages. And
 95 finally, it is also possible that the geomagnetic field is not in fact GAD-like but has long-
 96 term non-axial dipole contributions (as suggested by Wilson, 1970; Cromwell et al., 2013;
 97 Tauxe et al., 2022).

98 Paleomagnetists have identified behaviors in a paleointensity experiment that devi-
 99 ate from theoretical expectations and may lead to bias and recent studies have made
 100 a greater effort to eliminate such biased results. In most paleointensity studies, results
 101 from paleomagnetic specimens are excluded from the analysis if they fail a set of “selec-
 102 tion criteria” which are phenomenological descriptions of these behaviors. Alternatively,
 103 the BiCEP method (Cych et al., 2021) attempts to find a relationship between the ap-
 104 parent paleointensity and one of these commonly used selection criteria (curvature, Paterson,
 105 2011), and attempts to correct for the bias induced by the non-ideal behavior, obtain-
 106 ing accurate results without excluding data from the analysis based on arbitrary crite-
 107 ria. Recently, a study (Tauxe et al., 2022) which used the strict CCRIT criteria (Cromwell
 108 et al., 2015) and the BiCEP method on paleointensity studies from several latitudes found
 109 that there is still a discrepancy between these time-averaged paleointensities and those
 110 expected for a GAD field, making our first hypothesis (apparent non-dipole behavior is
 111 caused by bias in paleointensity estimation) unlikely to be the cause of inaccurate paleo-
 112 intensities.

113 Figure 1b shows the age distribution of latitudinally binned absolute paleointen-
 114 sity data in the MagIC database (without selection). It is apparent that different lati-
 115 tude bins have different age distributions. Because of this, the average paleointensity
 116 from each bin is representative of a different time period, and is not an average paleoin-
 117 tensity for the whole of the last 5 Ma. High quality paleointensity data, analyzed in a
 118 consistent manner, are needed to determine whether temporal sampling is the cause of
 119 apparent non-dipolar behavior, or if the time-averaged field is truly non-dipolar, as out-
 120 lined in our third hypothesis.

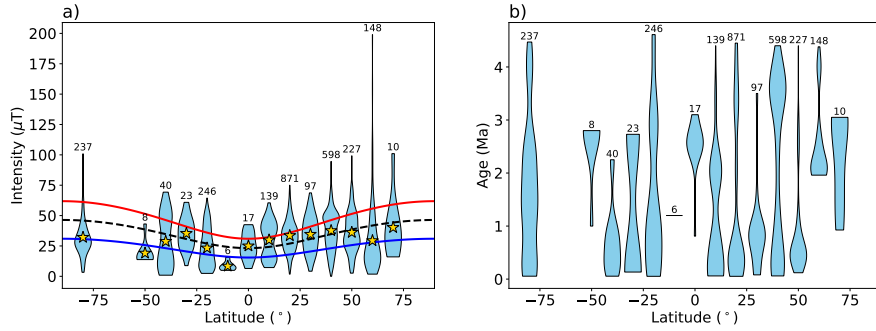


Figure 1. Violin plots showing latitudinal binned distributions of a) paleointensity and b) age for reported paleointensity results from the MagIC database aged between 50 ka and 5 Ma. In a violin plot, the width of the violin represents the frequency of intensities in that latitude bin, with the widest point in the violin representing the modal value. The number of data points in each bin are noted above the violins. The yellow stars in a) are the mean paleointensity value at each latitude bin and the solid blue, dashed black and solid red lines represent the expected mean values for a dipole field with a strength of 40, 60 and 80 ZAm^2 respectively.

121 In this paper, we present paleointensity estimates from rapidly cooled volcanic material from lava flows, dikes and vent deposits (scoria and spatter cones) aged 0-4 Ma
 122 from the Hawai‘ian islands. In Section 2, we describe how we collect samples in the field
 123 (2.1), how we conduct paleointensity experiments (2.2) on specimens therefrom, how we
 124 analyze our results using the BiCEP method which produces accurate estimates for spec-
 125 imens magnetized in known fields (2.3), and how we obtain ages for our samples using
 126 $^{40}\text{Ar}/^{39}\text{Ar}$ dating (2.4). In Section 3, we show the results of our paleointensity study in
 127 Hawai‘i. Section 4.2 discusses how our results suggest that scoria may be a useful lithol-
 128 ogy for obtaining high quality paleointensity estimates, and are in agreement with es-
 129 timates from other lithologies. In Section 4.3 we fit a model to our paleointensity data
 130 in an attempt to derive a time average that accounts for uneven temporal sampling. We
 131 then apply the same methodology to studies from Northern Israel and Antarctica. This
 132 allows us to test whether poor temporal sampling or non dipole behavior is responsible
 133 for the weaker paleointensity at high latitudes. Our results indicate that there is a per-
 134 sistent non-dipole component in the Earth’s magnetic field over at least the past 1.5 Ma
 135 with older data being much more consistent with a GAD field.
 136

137 2 Methods

138 2.1 Field Methods

139 Our results come from samples collected over three field seasons from outcrops on
 140 the Hawai‘ian islands. Samples were collected from the islands of Hawai‘i, Maui, Moloka‘i,
 141 and O‘ahu in an attempt to get a representative average paleointensity over the past 4
 142 Ma. This study targeted predominantly glassy and fine grained igneous material from
 143 lava flow tops and bottoms, scoria cones and dike margins. Néel theory (Néel, 1949) pre-
 144 dicted the physics of “uniaxial single domain” grains which should behave ideally in a pa-
 145 leointensity experiment. Only very small magnetic particle sizes exhibit single domain
 146 behavior, and so we sampled rapidly cooled materials most likely to contain these fine
 147 grains.

148 In the field, we collected small unoriented hand samples using a hammer and chisel;
 149 this allowed us to obtain smaller pieces of material and was less destructive than obtain-

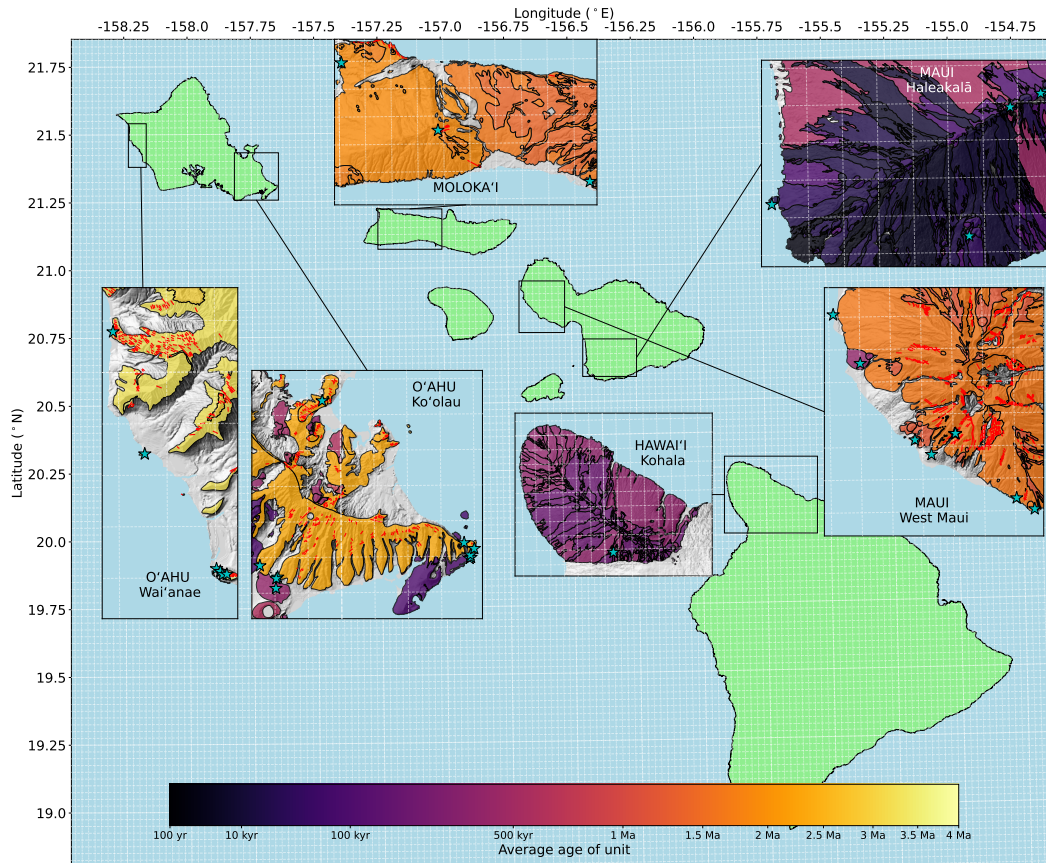


Figure 2. Maps showing sampling localities for successful sites used in this study (blue stars). Insets are labeled with the name of each island in capital letters and the name of the volcano (if applicable) in lowercase. Each map shows samples from a different Volcano/Island. Colors represent ages of units (Sherrod et al., 2007), with darker colors indicating younger flows (see colorbar), and dike locations indicated by red lines. Topographic data: U.S. Geological Survey (USGS). 2015. USGS 10-m Digital Elevation Model (DEM): Hawai'i. Coastline data: Hawai'i Statewide GIS Program.

150 ing oriented specimens with a drill. Maps of our sampling localities are shown in Fig-
 151 ure 2 and details regarding location, age and material are given in Table 1.

152 2.2 Laboratory Work

153 Each sample was crushed with a mortar and pestle to produce multiple paleomag-
 154 netic specimens with masses on the order of 0.1 g. Specimens were weighed and glued
 155 into 1 cm wide borosilicate glass tubes using a high temperature, low magnetic moment
 156 glue (KaSil). We subjected each specimen to the IZZI-Thellier method (Tauxe & Staudigel,
 157 2004; Yu et al., 2004). This is a step-wise double heating experiment in which the
 158 NRM is replaced by a Thermal Remanent Magnetization (TRM) acquired in a known
 159 lab field. Under the IZZI protocol, the order of the in-field and zero-field steps alternates
 160 at each temperature step. Under ideal conditions, the ratio of the magnetization lost in
 161 a zero-field step to the magnetization gained in an in-field step is the ratio of the ancient
 162 field (B_{anc}) to the laboratory field (B_{lab}). For this study, multiple lab fields were used

Table 1. Ages and locations for sites from this study that passed CCRIT or BiCEP. Locations for all sites, including those that did not pass CCRIT or BiCEP are listed in the supporting information. Latitudes and Longitudes are referenced to the WGS84 standard.

Site	Island	Lithology	Lat. (°N)	Lon. (°E)	Age (Ma)	$\pm 2\sigma$
HW306	Hawai'i	Vent Deposit	20.04470	-155.73437	0.1900	0.0700
ML001	Moloka'i	Dike	21.13719	-157.15547	2.0700	0.0200
ML012	Moloka'i	Vent Deposit	21.08955	-157.01053	1.6100	0.0300
ML015	Moloka'i	Vent Deposit	21.19876	-157.24734	1.7700	0.0200
MU004	Maui	Vent Deposit	20.77605	-156.53433	1.4300	0.0200
MU009	Maui	Vent Deposit	20.81885	-156.61782	0.6100	0.0120
MU011	Maui	Vent Deposit	20.83016	-156.63110	1.2300	0.0690
MU012	Maui	Vent Deposit	20.88931	-156.67484	0.3000	0.0216
MU013	Maui	Vent Deposit	20.92685	-156.69633	0.5840	0.0100
MU023	Maui	Vent Deposit	20.61085	-156.31100	0.0765	0.0635
MU025	Maui	Vent Deposit	20.70692	-156.25424	0.0950	0.0450
MU027	Maui	Vent Deposit	20.70551	-156.25857	0.0950	0.0450
MU031	Maui	Vent Deposit	20.69669	-156.28040	0.0670	0.0404
MU036	Maui	Vent Deposit	20.63397	-156.45102	0.0106	0.0085
MU106	Maui	Dike	20.83446	-156.59879	1.4900	0.0500
MU109	Maui	Dike	20.83440	-156.59798	1.5500	0.0500
MU111	Maui	Dike	20.83471	-156.59808	1.4500	0.0600
MU113	Maui	Lava Flow	20.78467	-156.54893	1.1000	0.0600
OA003	O'ahu	Flow	21.29434	-157.81123	2.5500	0.0800
OA008	O'ahu	Flow	21.40440	-158.17461	3.7100	0.0600
OA014	O'ahu	Dike	21.51972	-158.22772	3.4900	0.1700
OA015	O'ahu	Flow	21.46033	-158.21154	3.1000	0.0300
OA019	O'ahu	Flow	21.30938	-157.65783	2.8400	0.0600
OA026	O'ahu	Flow	21.29836	-157.65380	2.7700	0.1300
OA028	O'ahu	Flow	21.29907	-157.65273	2.7200	0.0800
OA030	O'ahu	Vent Deposit	21.27831	-157.79929	0.3800	0.1100
OA100	O'ahu	Vent Deposit	21.28628	-157.79791	0.4800	0.0400
OA101	O'ahu	Vent Deposit	21.28521	-157.79900	0.4800	0.0400
OA104	O'ahu	Flow	21.30080	-157.65320	2.1800	0.3500
OA108	O'ahu	Dike	21.30527	-157.65027	2.2500	0.1700
OA114	O'ahu	Dike	21.41002	-157.76354	2.8700	0.0600
OA116	O'ahu	Dike	21.40308	-158.17264	3.7200	0.0500
OA117	O'ahu	Dike	21.40308	-158.17264	3.7200	0.0500
OA123	O'ahu	Sill Margin?	21.40149	-158.17141	2.5900	0.0900
OA124	O'ahu	Dike	21.40168	-158.16927	3.2500	0.0100

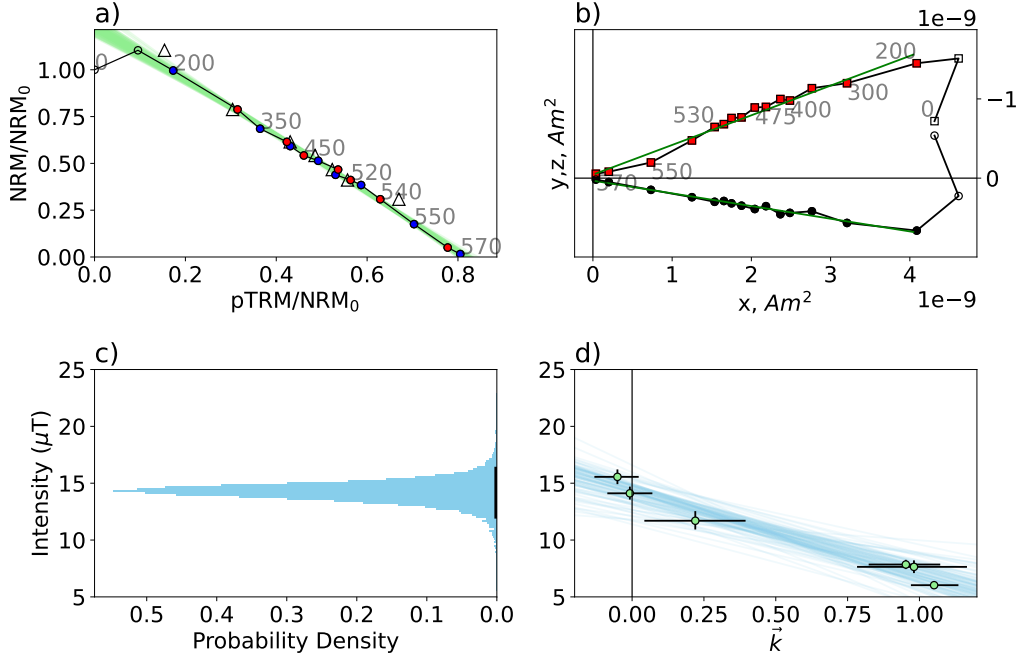


Figure 3. Example of BiCEP being used to obtain a paleointensity for site MU111. a) Arai plot (Nagata et al., 1963) for specimen MU111A05, red dots represent steps where the zero-field measurement was made first, and blue dots represent in-field first steps. Open circles represent temperature steps not used for this analysis. Triangles are pTRM checks and green curves are BiCEP’s circular fits to the data. b) Zijdeveld plot (Zijdeveld, 1967) showing magnetic direction data. Open symbols are steps where the temperature steps were not used. Green line is a principal component analysis fit to the directional data. c) Histogram of possible site mean intensities from BiCEP. d) BiCEP fit showing the predicted relationship (blue lines) between intensity (y axis) and the curvature criterion (\vec{k} , x axis).

163 for different specimens, as we observed that the choice of B_{lab} affected whether our specimens
 164 passed or failed some of our criteria (see Section 2.3).

165 **2.3 Analysis of Data**

166 To make sure that we have unbiased results, we used two different analysis meth-
 167 ods on our data to obtain an estimate of the ancient field. Primarily, we used the Bi-
 168 CEP method (Cych et al., 2021) of estimating paleointensities, but we also looked at re-
 169 sults using the CCRIT criteria of Cromwell et al. (2015). BiCEP assumes that the mag-
 170 netization records a single field, and thermochemical alteration of the specimen has not
 171 occurred. To make certain of this, we used the minimal selection criteria (see Paterson
 172 et al., 2014 for definitions and references), $DANG < 10$, $DRAT < 10$. In addition, we use
 173 a new parameter, $MAD_{C_{Oe}} < 5$ which just uses the zero-field first steps. The set of tem-
 174 perature steps on the Arai plot which maximize the FRAC criterion while passing the
 175 $MAD_{C_{Oe}}$, $DANG$ and $DRAT$ criteria. The vast majority of our specimens pass these
 176 criteria with ease, and the ones that do not would unambiguously be rejected by almost
 177 any other set of criteria. Site results from BiCEP have a 95% credible interval which is
 178 equivalent to the full width of the 2σ interval from traditional selection criteria meth-
 179 ods (e.g., CCRIT). We considered a site level result from BiCEP acceptable if it has a

180 credible interval with a full width less than 40% of the median value, or 16 μT , whichever
 181 is greater (the original BiCEP A or B criteria of Cych et al., 2021 only include the for-
 182 mer criterion). This is equivalent to criteria of $\pm 10\%$ or 4 μT used for the CCRIT at a
 183 site level. An example of BiCEP being used to estimate B_{anc} and its uncertainty for a
 184 site is shown in Figure 3.

185 2.4 Age Constraints

186 We obtained a range of radiometric ages for our samples that span the past 4 Ma.
 187 Rocks from 23 of our successful sites were analyzed at the Argon Geochronology lab at
 188 Oregon State University (OSU) for age determination. 200-300 μm pieces from each sam-
 189 ple were prepared by acid leaching in an ultrasonic bath according to the procedure of
 190 Koppers et al. (2000). This was followed by irradiation of the samples in the OSU TRIGA
 191 CLICIT nuclear reactor. Samples were then incrementally heated using a defocused CO_2
 192 laser, and the isotopic composition of the released argon was measured using an ARGUS-
 193 VI multi-collector mass spectrometer. Seventeen of our ages were calculated using argon-
 194 argon (Ar-Ar) plateaus. Three ages from sites OA019, OA116 and OA124 were calcu-
 195 lated using Mini-Plateau ages. Sites MU011 and MU036 were calculated using inverse
 196 isochron ages and site ML001 was calculated using a total fusion age. For sites OA030,
 197 OA100 and OA101, we used existing potassium-argon (K-Ar) ages (Ozawa et al., 2005),
 198 and on West Maui, existing K-Ar ages (Tagami et al., 2003) were similarly used for sites
 199 MU009 and MU013. Mapped scoria cones at sites MU023, MU025 and MU027 have good
 200 age constraints over the timescale we are interested in from K-Ar dating and stratigraphic
 201 relationships outlined in Sherrod et al. (2003). Finally, site OA026 has its age constrained
 202 by stratigraphic relationship with our other Ar-Ar dated flows. A full table of ages is given
 203 in Table 1.

204 3 Results

205 Results are listed in Table 2. We obtain passing results from 35 sites (Table 2): 31
 206 passed BiCEP and 21 passed CCRIT. Some of the results that pass CCRIT do not pass
 207 BiCEP, but those sites that pass both methods exhibit good agreement between one an-
 208 other. Because BiCEP gives a more objective analysis, and because we obtain more pass-
 209 ing results with this method, we use only the results that pass BiCEP for the rest of our
 210 analyses.

211 We plot our results versus age in Figure 4. It is apparent that our results support
 212 the hypothesis that the more recent field (over the past ~ 1.5 Ma) is considerably higher
 213 than that from 1.5-4 Ma (e.g., Tauxe, 2006), supporting the hypothesis of a potential
 214 long period variation in the field strength (Selkin & Tauxe, 2000; Tauxe, 2006; Ziegler
 215 et al., 2011). It is also worth noting that in Figure 1, latitudes which have age distribu-
 216 tions which skew towards ages older than 1 Ma (e.g., 80°S , 60°N , 0°) tend to have av-
 217 erages that agree with a ~ 40 ZAm^2 dipole, whereas the majority of latitudes with mostly
 218 younger results tend to agree with a 60-70 ZAm^2 dipole moment, so qualitatively our
 219 hypothesis that the missing dipole may be caused by temporal sampling seems plausi-
 220 ble. However, the data from Antarctica (Asefaw et al., 2021) span the entire last 4 Ma
 221 but also have an average field consistent with a 40 ZAm^2 axial dipole strength, so tem-
 222 poral sampling alone does not explain all of the deviation from a GAD field.

223 The high paleointensity results over the past 1.5 Ma come predominantly from vent
 224 deposits (scoria and spatter cones), whereas older results come predominantly from dikes
 225 and lava flows. The dikes and lava flows are associated with the early shield building stages
 226 of Hawai'ian volcanoes, whereas the vent deposits are predominantly from the later stages
 227 of volcanic construction. The difference in lithology being coupled with a difference in
 228 field strength may be concerning, however our young, high field strength results agree
 229 well with the average paleointensity from lava flows in the HSDP2 core (Cai et al., 2017;

Table 2. Paleointensity results from specimens in this study which passed BiCEP and CCRIT. n_{pass} : Number of passing specimens. n_{tot} : Total number of specimens. For CCRIT results B_{min} and B_{max} represent the bounds of the 2σ interval, and so a full width of 40% or 16 μT is considered to have passed. The method column represents the preferred paleointensity result (BiCEP) when a site passed both BiCEP and CCRIT

Site	n_{pass}/n_{tot}	B_{min}	B_{anc}	B_{max}	Method
HW306	8/8	30.8	36.8	42.9	BiCEP
ML001	7/7	23.2	31.2	39.2	BiCEP
ML012	6/6	28.1	29.0	30.2	BiCEP
ML015	5/5	5.5	12.0	16.7	BiCEP
MU004	11/11	39.3	42.3	45.5	BiCEP
MU009	6/6	31.1	36.6	42.4	BiCEP
MU011	5/9	19.2	26.5	33.8	CCRIT
MU012	6/6	31.8	34.6	37.6	BiCEP
MU013	8/8	14.8	19.2	23.8	BiCEP
MU023	8/8	26.1	31.0	35.6	BiCEP
MU025	7/7	33.9	42.1	50.2	BiCEP
MU027	6/6	19.7	24.7	30.7	CCRIT
MU031	10/10	34.6	40.4	46.0	BiCEP
MU036	9/9	10.4	10.9	11.4	BiCEP
MU106	10/12	22.1	28.8	35.0	BiCEP
MU109	7/7	15.9	18.8	21.9	BiCEP
MU111	6/6	12.1	14.3	16.2	BiCEP
MU113	8/8	38.1	43.7	49.7	BiCEP
OA003	11/11	26.9	29.2	31.3	BiCEP
OA008	4/4	14.9	20.2	26.2	BiCEP
OA014	10/12	10.3	13.0	15.6	BiCEP
OA015	8/8	35.3	39.7	44.5	BiCEP
OA019	15/15	20.5	22.9	25.3	BiCEP
OA026	8/8	12.5	15.0	17.4	BiCEP
OA028	8/8	29.4	33.1	36.8	BiCEP
OA030	16/16	45.6	48.9	52.2	BiCEP
OA100	6/12	50.0	51.0	52.0	CCRIT
OA101	9/9	37.3	43.0	48.3	BiCEP
OA104	3/8	15.8	17.6	19.3	CCRIT
OA108	8/8	13.2	19.5	25.5	BiCEP
OA114	6/6	21.8	25.3	30.2	BiCEP
OA116	8/8	21.7	24.9	28.2	BiCEP
OA117	5/5	19.2	23.7	28.1	BiCEP
OA123	6/8	10.3	13.8	19.0	BiCEP
OA124	7/7	33.8	36.8	40.2	BiCEP

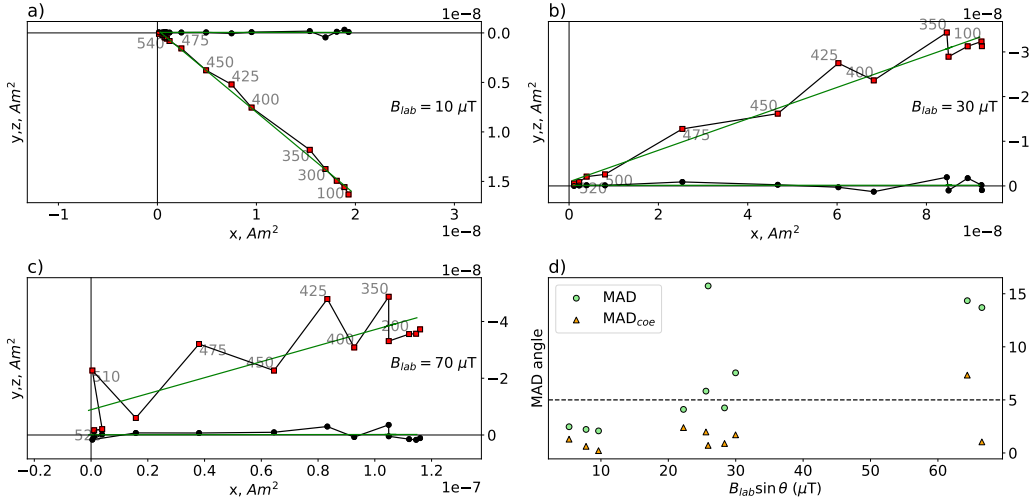


Figure 5. a)-c) Zijderveld plots of specimens from site OA014, showing zig-zagging behavior that progressively increases with lab field and d) Scatter plot showing the relationship between the MAD criterion, and the magnitude and angle of the lab field for all ten fully demagnetized specimens from this site. Paleointensity experiments were performed laboratory fields of a) a 10 μT , b) 30 μT and c) 70 μT . d) MAD (green circles) angle against the strength of the component of the lab field perpendicular to the ancient field direction (calculated by the PCA of the zero-field first steps). Orange triangles are the MAD of the zero-field first steps only (MAD_{Coe}). Horizontal dashed line represents the selection criterion (5) used in this study. Using MAD_{Coe} improves, though does not completely eliminate, the lab-field dependence of MAD. All MADs were calculated using temperature steps above 400-600°C to avoid any potential viscous remanent magnetization (VRM).

230 Tauxe & Love, 2003, reanalyzed in Tauxe et al., 2022), shown as grey triangles in Fig-
 231 ure 4, although the variance of the HSDP2 data is larger. Additionally, results from sev-
 232 eral scoria cones yielded much weaker fields, including for two cones on Moloka'i older
 233 than 1.5 Ma. This leads us to believe that our results from scoria are accurate.

234 4 Discussion

235 4.1 Pitfalls of selection criteria

236 We used the BiCEP method to obtain site level paleointensity estimates, and pre-
 237 fer this over the CCRIT method (and all other sets of selection criteria in use by var-
 238 ious authors) as BiCEP produces many more site level results than CCRIT. Often, Bi-
 239 CEP passed sites where specimens failed the FRAC criterion of CCRIT, which speci-
 240 fies that a large proportion of the total magnetization of the specimen is needed to make
 241 a paleointensity estimate. BiCEP accounts for the uncertainty in curvature (and there-
 242 fore bias), introduced by using only part of a specimen's Arai plot for a paleointensity
 243 estimate. This can be seen in Figure 3a, where specimen MU111A05 fails CCRIT due
 244 to low FRAC, but using a smaller part of the Arai plot translates to only a small increase
 245 in the uncertainty in curvature, shown by the green curves fit to the data.

246 In addition to the FRAC criterion in CCRIT, we identify cases in which criteria
 247 may reject a specimen if it has an ancient field much lower than the lab field. The MAD

248 criterion may be exceeded if the laboratory magnetization acquired in an in-field step
 249 is not fully removed during a zero-field step, a consequence of a “high temperature pTRM
 250 tail” (Dunlop & Özdemir, 2000). This behavior is very noticeable in IZZI experiments
 251 (Figure 5), as the in-field first steps are more strongly affected by this effect. This leads
 252 to a zig-zag appearance in the Zijderveld plot. The sizes of these tails are dependent on
 253 both the magnitude of the lab field, and the effect the tails have on MAD is dependent
 254 on the angle between lab and ancient field. If we call this angle θ , then the perpendicular
 255 part of the tails will be controlled by $B_{lab} \sin \theta$. If we assume no other sources of
 256 deflection to the MAD angle, the equation for the effect is:

$$\tan(\text{MAD}) \propto \frac{B_{lab}}{B_{anc}} \sin \theta. \quad (1)$$

257 This equation demonstrates that in the same lab field, sites with low ancient fields will
 258 be preferentially rejected with higher MAD, and sites with high ancient fields will be pref-
 259 erentially accepted.

260 To counteract the lab field-dependent effects, we used 10, 30 and 70 μT fields in
 261 our studies, which captures the range of the ancient field. At some sites with low esti-
 262 mated B_{anc} , there was an observably higher pass rate in lower fields. An example of this
 263 for site OA014 is illustrated in Figure 5. To treat specimens magnetized in different fields
 264 fairly, it is tempting to come up with a criterion for MAD which is dependent on Equa-
 265 tion 1. However, effects that we may be using MAD to look for (e.g., two component mag-
 266 netizations) will not be dependent on the lab field, and so we suggest calculating MAD
 267 for exclusively the zero-field first or “Coe” type steps (Coe, 1967). Although pTRM tails
 268 may still be present in these steps, they will be significantly reduced in in-field first steps.
 269 We call a MAD calculated using these steps MAD_{Coe} and how it compares to MAD for
 270 site OA014 is shown in Figure 5d. This significantly reduces the lab field-dependent ef-
 271 fects, but does not eliminate them entirely. Because pTRMs scale with the lab field used,
 272 there may be other unrecognized pTRM dependent effects. We recommend using a range
 273 of lab fields in paleointensity studies as the most robust way of compensating for these
 274 effects.

275 4.2 Sample Characterization

276 We have demonstrated our ability to obtain high quality paleointensity results from
 277 our samples using the BiCEP method. However, it is not clear what the primary car-
 278 riers of the magnetization are for these samples, particularly for samples from vent de-
 279 posits, which are relatively unstudied in the paleointensity literature. To attempt to char-
 280 acterize the domain state of our samples, we obtained First Order Reversal Curves (FORCs,
 281 (Pike et al., 1999)) using the xFORC protocol of Zhao et al. (2017) on selected mate-
 282 rial from sites which passed BiCEP (and from some which failed). For this analysis we
 283 used sister specimens from the same samples for which the paleointensity results were
 284 acquired. FORCs are a qualitative way of assessing the domain state of a specimen us-
 285 ing its hysteresis properties. Specimens which contain “Single-Domain” (SD) grains which
 286 are ideal for the paleointensity experiment will have FORCs with a central ridge of pos-
 287 itive values along the $H_a = -H_b$ axis (see e.g., Figure 6a). Specimens with higher num-
 288 bers of non SD grains will have FORCs which have a spread along the $H_a = H_b$ axis. The
 289 iFORC which represents the induced part of the magnetization displays a pattern of three
 290 distinct “lobes” (e.g., Figure 6b,e) for a sample containing SD grains, whereas it may
 291 display four “lobes” or be extremely noisy for samples containing non-SD grains. The
 292 tFORC represents “transient hysteresis” which occurs in non-SD grains; specimens with
 293 just noise on the tFORC (e.g., Figure 6c) are most likely to be single domain.

294 Examples of FORCs and Arai plots for different samples are displayed in Figure 6.
 295 The FORC interpretations generally agree with the paleointensity experimental results.
 296 FORCs obtained from dike samples have pronounced central ridges and three lobes in
 297 the iFORC if visible, and effectively no tFORC (Figure 6a-d). These samples generally

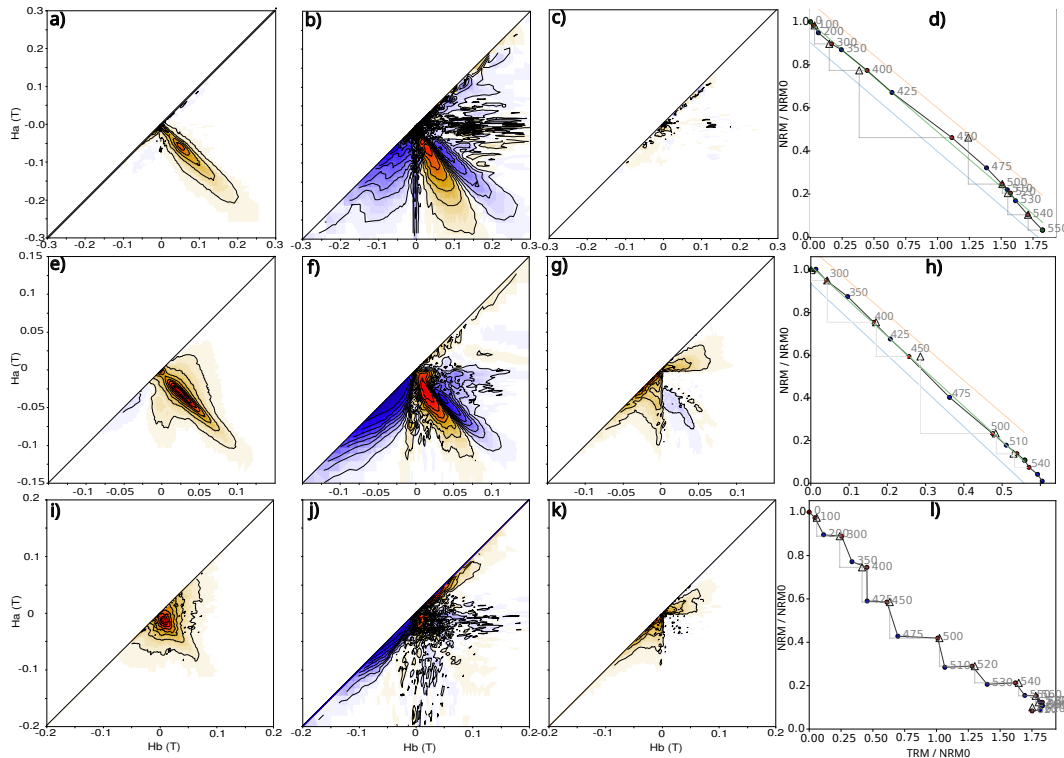


Figure 6. First Order Reversal Curves (FORCs a),e),i), iFORCs b),f),j), and tFORCs c),g),k) calculated using the xFORC protocol (Zhao et al., 2017). All FORCs calculated using a smoothing factor of 2 and a non-linear color scale of 1, except for iFORCs which were calculated using a smoothing factor of 3 and a non-linear color scale of 10. Arai plots are plotted in d),h),k). FORCs use sister specimens from two sites that yielded passing results: OA030 (top row), OA014 (center row) and a site which did not pass CCRIT or BiCEP, HW305 (bottom row). Sites which yielded specimens with linear Arai plots tend to have an elongated central ridge and have 3 lobes in the iFORC (top and center rows), whereas sites with curved Arai plots tend to have more spread along the $H_a = H_b$ direction and have extremely noisy iFORCs with little information.

298 had Arai plots which were straight lines, but sometimes underwent thermochemical
 299 alteration at high temperatures. Samples from lava flows and vent deposits had central
 300 ridges, with small amounts of transient hysteresis and spreading along the $H_a = H_b$
 301 axis. These samples still have linear Arai plots, and often have three lobes present in the
 302 iFORC, which suggests that the majority of carriers in these specimens are single do-
 303 main (see Figure 6e-h). An example from a relatively coarse grained lava flow is given
 304 in Figure 6i-l. Samples like these had highly curved or zig-zagging Arai plots (Figure 6l)
 305 generally had no central ridge and lots of spreading along the $H_a = H_b$ axis (Figure 6i).
 306 These samples had pronounced tFORCs (Figure 6k), and only noise in the iFORCs away
 307 from the H_a axis (Figure 6j), observations which are consistent with the curved and zig-
 308 zagging Arai plots.

309 We also obtained Back Scattered Electron (BSE) images using an Scanning Elec-
 310 tron Microscope (SEM), and Electron Dispersive X-Ray Spectroscopy (EDS) element
 311 maps to identify iron oxides in several thin sections taken from our samples. Several pic-
 312 tures from these analyses are displayed Figure 7. Dike samples we analyzed contained
 313 no visible iron oxides in the glass, and almost no iron oxides in the groundmass. This
 314 is consistent with our FORCs and Arai plots (Figure 6a-d), which are indicative of this

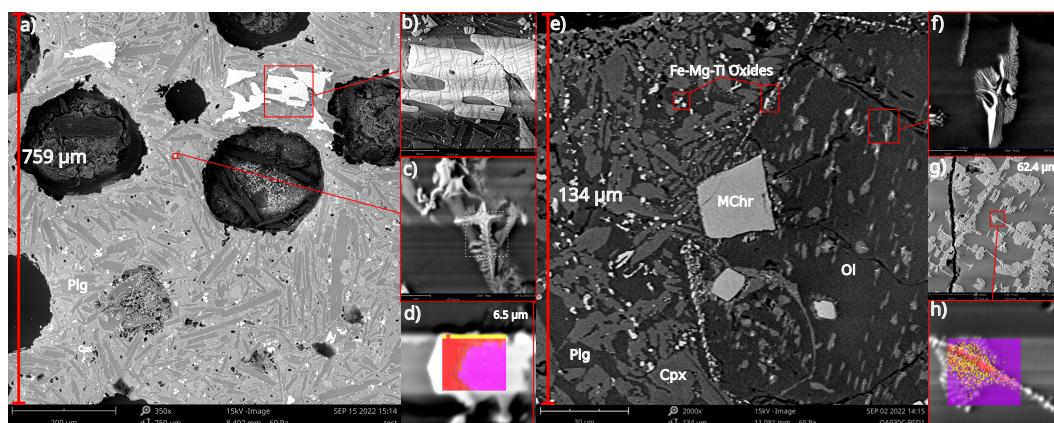


Figure 7. Back Scattered Electron (BSE) images and Electron Dispersive X-Ray Spectroscopy (EDS) maps of sister specimens from selected samples used in this study. Red text gives vertical field of view (FOV) for each image. a) BSE image of sample ML015A, a scoria vent deposit. b) Zoomed in image of large oxide in a), showing Fe-Ti exsolution textures. c) Zoomed in image of small oxide in a), showing elongate skeletal/cruciform structure. d) EDS element map of a typical oxide from another scoria vent deposit, ML012A, showing heterogeneous composition in the Iron-Titanium oxides. The atomic content of Si is shown in yellow, Fe in red, and Ti in pink. e) BSE image of sample OA030A, an agglutinated basanite vent deposit. f) Close up of high temperature alteration texture in olivine phenocryst. g) The same texture present in sample MU012A, a breccia from the bottom of a basanite lava flow. h) Close up of this texture with EDS element map. Colors are the same as d), with purple representing Mg. Note that the light colors in the BSE image represent an iron rich phase (interpreted as magnetite), which is surrounded by a phase richer in silicon than the surrounding olivine, interpreted as enstatite. Dominant mineral phases written on a) and e): Plg: plagioclase feldspar, Cpx: clinopyroxene, Ol: olivine, MChr: chrome spinel. Horizontal banding present in b),c),d),f),h) is an artifact of charging the sample that occurs in the SEM's EDS element mapping mode.

315 specimen containing a predominance of single domain grains, which are 10s of nm in scale
 316 and not resolvable by the SEM used in this analysis. By contrast, samples from vent de-
 317 posits contained numerous micron-scale iron bearing oxides in the groundmass, and in
 318 some cases, larger iron oxides on the scales of 100s of microns (Figure 7a-d), size ranges
 319 where we would expect the grains to yield curved Arai plots. Many of these grains have
 320 elongated “cruciform” textures (Figure 7c) or have heterogeneous compositions (Figure 7a,d).
 321 One possibility is that these textures may persist to smaller scales, causing the larger
 322 grains to behave like assemblages of smaller, single domain, grains, due to their elonga-
 323 tion or having smaller magnetic subregions separated by nonmagnetic lamellae. Another
 324 possibility is that these large grains do not contribute to the remanence. However, the
 325 lava flows and vent deposits have much higher NRM moments than the dikes, with mass
 326 normalized NRMs on the order of 10^{-2} to 10^{-3} Am²/kg, as opposed to the dikes which
 327 have moments on the order of 10^{-4} to 10^{-5} Am²/kg.

328 Two thin sections from sites MU012 and OA030 have numerous olivine grains which
 329 exhibit an unusual texture, as displayed in Figure 7e-h. This texture has been observed
 330 previously (Ejima et al., 2017; Blondes et al., 2012) and is interpreted as being caused
 331 by oxidation of olivine at temperatures above 800°C, which causes breakdown into an
 332 iron oxide (magnetite or hematite depending on formation conditions) and enstatite (see
 333 Figure 7h and figure caption). The temperature of the oxidation means that the sam-
 334 ples were oxidized prior to gaining a magnetization, which means the NRM is a primary
 335 TRM acquired during cooling. Oxidation of this kind seems to typically occur in fire foun-
 336 taining strombolian type eruptions (e.g., Del Moro et al., 2013) where the lavas remain
 337 at high temperatures in an oxidizing environment for a while (e.g., 950 °C for 24-48 hours
 338 as per (Haggerty & Baker, 1967)). OA030 is an agglutinated basanitic vent deposit, agree-
 339 ing with this oxidative environment, whereas the MU012 sample was taken from brec-
 340 cia/clinkers in an a‘ā lava flow, which may also undergo high temperature oxidation al-
 341 though the source is less clear.

342 Both sites with evidence for high temperature oxidation of olivines had highly lin-
 343 ear Arai plots (see Figure 6h), with 16/16 specimens passing the strict CCRIT criteria
 344 for OA030, and 6/6 passing for MU012. Additionally a sample from OA030 has a FORC
 345 indicative of single-domain to single-vortex domain state, with a central ridge and three
 346 lobes in the iFORC (see Figure 6, middle row). This indicates that the oxides formed
 347 by this breakdown may have extremely desirable properties for paleointensity experiments.
 348 Similar to the smaller oxides found in our other vent deposits (Figure 7c), the elonga-
 349 tion and finger-like structures present in these oxides could also explain their ideal be-
 350 havior in the paleointensity experiment. These thin sections also contained numerous
 351 micron scale iron-titanium-magnesium oxides (interpreted as magnesioferrite) in the ground-
 352 mass and around the outside of the olivine grains (Figure 7e), but because the major-
 353 ity of the remanence unblocks between 400 and 600°C (see Figure 6d), we believe that
 354 magnetite is the dominant remanence carrier in these specimens.

355 Despite the large iron oxides observed in vent deposits and lava flows from this study,
 356 we conclude that these lithologies provide a good source for paleointensity estimates, as
 357 they have a high success rate relative to our other lithologies owing to their strikingly
 358 linear Arai plots (see Figure 6, top row). Site MU113 provides further evidence for this,
 359 as material sampled from the inside of a lava tube gave an identical result to material
 360 sampled from a scoriaceous bomb entrained in the same flow. There are other reasons
 361 to favour these types of lithologies: The formation of these samples in an oxic environ-
 362 ment at high temperature may help prevent thermochemical alteration during the pa-
 363 leointensity experiment, and fresh scoria is also easy to come by in Hawai‘i, as many sco-
 364 ria cones are quarried. However, most preserved vent deposits are typically formed dur-
 365 ing the later stages of Hawai‘ian volcanism, and consequently we have no results from
 366 scoria older than 2 Ma.

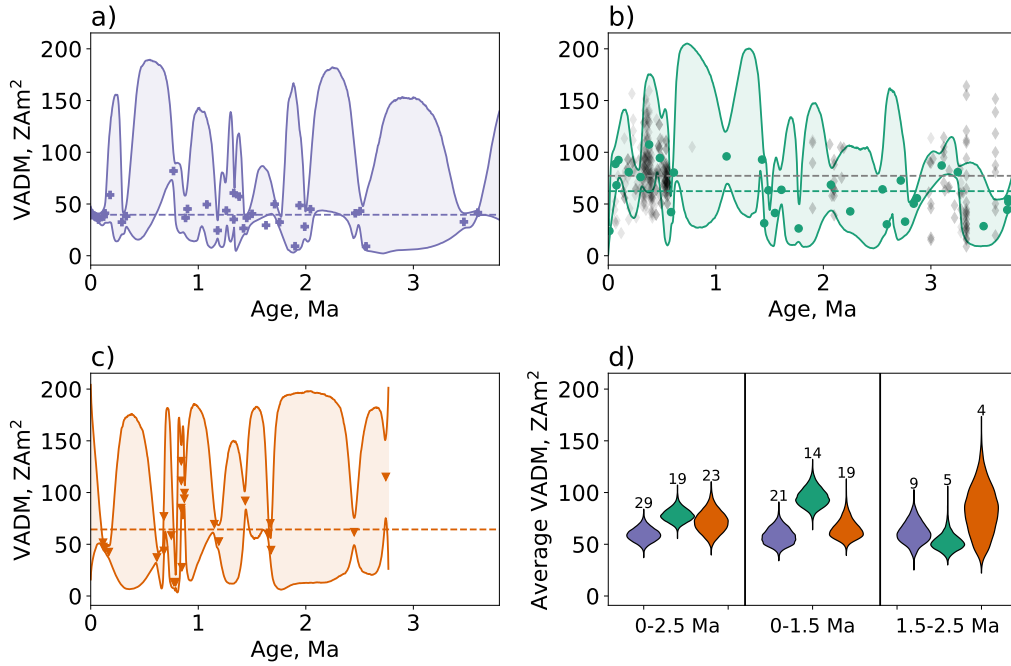


Figure 8. a) - c) Plots of VADM against age (symbols), and 95% credible envelopes for AH-RJMCMC models (Livermore et al., 2018) (shaded areas) for studies from a) Antarctica (purple plus symbols), b) Hawai'i (green dots), and c) Israel (orange triangles). Horizontal dashed lines are the average VADM of all paleointensity estimates (symbols) for each plot. In b), all unfiltered data in the MagIC database from Hawai'i aged between 50 ka and 3.8 Ma are plotted as grey diamonds, and the average VADM from these data are plotted as a grey horizontal line. d) Violin plots showing the distribution of averaged VADMs over different time periods, numbers refer to the number of paleointensity within these temporal ranges, although data outside these ranges may also contribute to these averages. Data from Hawai'i have a significantly higher average VADM than in Israel and Antarctica over the past 1.5 Ma, which is reflected in the averages from 0-2.5 Ma. Average VADMs for data older than 1.5 Ma appears to agree for all three locations.

367

4.3 Temporal Distributions of Intensity

368

369

370

371

372

373

374

375

376

377

378

379

380

381

382

Mismatch between the observed distribution of paleointensities with latitude and the expected distribution for a GAD field (Figure 1a) could potentially be caused by inconsistencies in treatment of data among different paleointensity studies. To compare the time-averaged field from our model to data from different latitudes, we reanalyzed results from recent paleomagnetic studies in Northern Israel (Tauxe et al., 2022) and Antarctica (Asefaw et al., 2021) using the BiCEP method and the same criteria used for the Hawai'i samples. Tables of results from these re-analyses can be found in the Supporting Information. Each of these studies yielded passing sites with results spanning the past 2.5 Ma. For direct comparisons between locations, we convert each paleointensity result to a Virtual Axial Dipole Moment (VADM) which is the moment of the geocentric dipole (measured in ZAm^2) that would yield the observed paleointensity at a given latitude. Our average VADM for Hawai'i is 62.4 ZAm^2 , which is similar to the 64.2 ZAm^2 value from Israel, but is significantly higher than the average in Antarctica (39.6 ZAm^2). Plots of VADMs with age for each location are shown in Figures 8a)-c), with average VADMs plotted as horizontal dashed lines. In Figure 8b we also plot all the data from Hawai'i

383 in the MagIC database from this time interval in grey. The unfiltered data have a sig-
 384 nificantly higher variance than our data, and the weaker field seen prior to 1.5 Ma in our
 385 data is not apparent in the unfiltered Hawai‘ian data, which have an average VADM of
 386 77.2 ZAm². These differences could occur because more field variation is being captured
 387 by the larger dataset, or because the unfiltered data have more variance due to incon-
 388 sistency in their analysis (for example, preferentially taking the low temperature steps
 389 in a potentially sagging Arai plot). Despite the consistency in analysis of our data, the
 390 average VADM in Hawai‘i and Israel is still very different to that found in Antarctica,
 391 indicating that inconsistency in analyses and biased paleointensities caused by Arai plot
 392 curvature are not the source of this mismatch.

393 Taking an average VADM of the entire age range of our data may not be represen-
 394 tative of the time-averaged field, because our data have different temporal distributions,
 395 with no data in Israel older than 2.75 Ma. In Hawai‘i, this average does not capture the
 396 change in average field strength seen at 1.5 Ma, and in Israel, we have many paleointen-
 397 sity data which record a strong field and come from a small range of time around 850
 398 ka B.P. Because this time interval is oversampled, it will bias our average VADM towards
 399 these higher values. To account for these problems, it would make sense to fit a curve
 400 to our VADMs and take an average of the curve over an interval of interest. We do this
 401 using the “Age Hyperparameter Reversible Jump Markov Chain Monte Carlo” (AH-RJMCMC)
 402 method (Livermore et al., 2018). This model fits piecewise linear curves to paleointen-
 403 sity data in a probabilistic fashion, with curves with less linear pieces being preferable
 404 for the model. At times when there are few data, the model uncertainties become very
 405 large and revert to a uniform prior distribution, which we set as 0-220 ZAm². At times
 406 where we have no data, the uncertainty in the average VADM will increase, and so any
 407 differences in the average VADM using this method are driven by the data.

408 We computed the AH-RJMCMC models, which output a series of possible piece-
 409 wise linear curves at each locality. We took the average value of each curve over the past
 410 2.5 Ma, and converted these averages to VADMs. The models produced by this anal-
 411 ysis are shown in Figure 8a-c, and the distributions of the time-averaged VADMs for each
 412 locality are plotted on the violin plots in Figure 8d. Using this methodology, it is appar-
 413 ent that the time-averaged VADMs over the last 1.5 Ma from Hawai‘i and Antarctica
 414 are indeed not consistent with each other, but the time-averaged VADM in Israel could
 415 be compatible with either of the other latitudes. However, there is not enough evidence
 416 to confirm a difference in the temporal average between Hawai‘i and Antarctica from 1.5-
 417 2.5 Ma, with the average VADMs appearing consistent. This implies that poor tempo-
 418 ral sampling is not the reason for inconsistent paleointensities at different latitudes, but
 419 that some form of genuine non-dipolar field behavior that causes higher fields in Hawai‘i
 420 than Antarctica at least since 1.5 Ma. More paleointensity studies with high quality pa-
 421 leointensity data at different latitudes (especially from the southern hemisphere) are needed
 422 to better understand the sources of this non-dipolar behavior.

423 5 Conclusions

424 In this paper, we obtained 31 high quality paleointensity results from dikes, lava
 425 flow tops and vent deposits collected in the Hawai‘ian islands, with ages ranging from
 426 0-4 Ma. We demonstrate a methodology for obtaining accurate time-averaged paleointen-
 427 sities, with uncertainties which allow direct comparison between paleointensity stud-
 428 ies at different latitudes. The use of BiCEP allows for consistent comparison of results
 429 between different studies, and using the methodology of Livermore et al. (2018) allows
 430 us to obtain a time-averaged intensity, with uncertainty, which accounts for the tempo-
 431 ral distribution of our paleointensity. Because these robust statistical approaches are used
 432 for calculating time-averaged paleointensities, we are able to exclude the hypotheses that
 433 inconsistency of our time-averaged VADMs is due to either biased paleointensity data,
 434 or inconsistent temporal sampling of paleointensities.

435 Applying the new methodology to data from the Hawai‘ian islands, we find that
 436 the time-averaged paleointensity in Hawai‘i over the past 1.5 Ma was higher than dur-
 437 ing the period from 1.5-4 Ma. Comparing results from paleointensity studies at three lat-
 438 itudes, we find that this period of high paleointensity is not recorded in rocks from Antarc-
 439 tica or Israel. We reiterate the conclusion of other recent papers (e.g., Tauxe et al., 2022)
 440 that the Earth’s magnetic field averaged over the past 1.5 Ma does not conform to a Geo-
 441 centric Axial Dipole. Further time averages at a greater range of latitudes and times will
 442 be needed to obtain better estimates of the structure of this time-averaged field.

443 Our results also indicate that vent deposits containing scoria, and olivine bearing
 444 rocks which are oxidized at high temperatures are potentially good lithologies for obtain-
 445 ing high quality paleointensity estimates, with higher success rates in the paleointensity
 446 experiment. Specimens from these lithologies have strong magnetizations and tend to
 447 alter less in paleointensity experiments. Additionally, these deposits are frequently quar-
 448 ried, allowing for easy access to fresh material in the field. Despite their useful proper-
 449 ties in paleointensity experiments, and their single-domain like FORCs, the size of iron
 450 oxides in these samples when viewed under a microscope is orders of magnitude larger
 451 than would be expected for single domain grains. Further study of the magnetic carri-
 452 ers in these samples should be undertaken to understand why they have such ideal rock
 453 magnetic properties.

454 6 Open Research

455 All data and interpretations are available at [https://earthref.org/MagIC/19614/
 456 9208acad-0f62-4d9e-b265-4c8907d40eb7](https://earthref.org/MagIC/19614/9208acad-0f62-4d9e-b265-4c8907d40eb7) and will be made available in the MagIC database
 457 at <http://earthref.org/MagIC/19614> on acceptance of this paper. Python notebooks
 458 for producing figures can be found at https://github.com/bcych/hawaiian_paleointensity.

459 Acknowledgments

460 This work was partially supported by EAR1827263 to LT and EAR1520788 to GC. We
 461 would like to thank the Hawai‘i Department of Land and Natural Resources’ Forestry
 462 and Wildlife Program for issuing sampling permits in West Maui, and Moloka‘i Ranch
 463 Ltd. and Moloka‘i Land Trust for allowing us to sample on their land. We are grateful
 464 for comments from Cathy Constable and Jeffery Gee which improved the manuscript.
 465 Finally we would like to thank the late Jasper Konter for his help in the field and hos-
 466 pitality during our field work on Oahu. He will be missed.

467 References

- 468 Asefaw, H., Tauxe, L., Koppers, A. A. P., & Staudigel, H. (2021, February). Four-
 469 dimensional paleomagnetic dataset: Plio-Pleistocene paleodirection and paleo-
 470 ointensity results from the Erebus Volcanic Province, Antarctica. *J. Geophys.*
 471 *Res. Solid Earth*, *126*(2), e2020JB020834. doi: 10.1029/2020JB020834
- 472 Blondes, M. S., Brandon, M. T., Reiners, P. W., Page, F. Z., & Kita, N. T. (2012,
 473 May). Generation of forsteritic olivine (Fo99-8) by subsolidus oxidation in
 474 basaltic flows. *J. Petrol.*, *53*(5), 971–984. doi: 10.1093/petrology/egs006
- 475 Cai, S., Tauxe, L., & Cromwell, G. (2017, November). Paleointensity from subaerial
 476 basaltic glasses from the second Hawaii Scientific Drilling Project (HSDP2)
 477 core and implications for possible bias in data from lava flow interiors. *J.*
 478 *Geophys. Res. Solid Earth*, *122*(11), 8664–8674. doi: 10.1002/2017JB014683
- 479 Coe, R. S. (1967). The determination of paleo-intensities of the earth’s magnetic
 480 field with emphasis on mechanisms which could cause non-ideal behavior in
 481 thellier’s method. *J. Geomag. Geoelectr.*, *19*, 157–178.
- 482 Cromwell, G., Johnson, C. L., Tauxe, L., Constable, C. G., & Jarboe, N. A. (2018,

- 483 May). PSV10: A global data set for 0–10 Ma time-averaged field and paleosec-
 484 ular variation studies. *Geochem. Geophys. Geosyst.*, *19*(5), 1533–1558. doi: 10
 485 .1002/2017GC007318
- 486 Cromwell, G., Tauxe, L., Staudigel, H., Constable, C. G., Koppers, A. A. P., & Ped-
 487 ersen, R.-B. (2013, August). In search of long-term hemispheric asymmetry
 488 in the geomagnetic field: Results from high northern latitudes. *Geochem.*
 489 *Geophys. Geosyst.*, *14*(8), 3234–3249. doi: 10.1002/ggge.20174
- 490 Cromwell, G., Tauxe, L., Staudigel, H., & Ron, H. (2015, April). Paleointensity
 491 estimates from historic and modern Hawaiian lava flows using glassy basalt
 492 as a primary source material. *Phys. Earth Planet. Inter.*, *241*, 44–56. doi:
 493 10.1016/j.pepi.2014.12.007
- 494 Cych, B., Morzfeld, M., & Tauxe, L. (2021, August). Bias Corrected Estimation
 495 of Paleointensity (BiCEP): An improved methodology for obtaining paleoin-
 496 tensity estimates. *Geochem. Geophys. Geosyst.*, *22*(8), e2021GC009755. doi:
 497 10.1029/2021GC009755
- 498 Del Moro, S., Renzulli, A., Landi, P., La Felice, S., & Rosi, M. (2013, March).
 499 Unusual lapilli tuff ejecta erupted at Stromboli during the 15 March 2007
 500 explosion shed light on the nature and thermal state of rocks forming the
 501 crater system of the volcano. *J. Volcanol. Geotherm. Res.*, *254*, 37–52. doi:
 502 10.1016/j.jvolgeores.2012.12.017
- 503 Dunlop, D., & Özdemir, O. (2000). Effect of grain size and domain state on thermal
 504 demagnetization tails. *Geophys. Res. Lett.*, *27*, 1311–1314.
- 505 Dunlop, D., & Özdemir, O. (2001). Beyond Néel’s theories: thermal demagnetization
 506 of narrow-band partial thermoremanent magnetization. *Phys. Earth Planet.*
 507 *Int.*, *126*, 43–57.
- 508 Ejima, T., Yoneda, M., Akasaka, M., Ohfuji, H., Kon, Y., Nagashima, M., & Naka-
 509 muta, Y. (2017). Precipitates within olivine phenocrysts in oxidized andesitic
 510 scoria from Kasayama volcano, Hagi, Japan. *J. Mineral. Petrol. Sci.*, *112*(3),
 511 116–126. doi: 10.2465/jmps.161219
- 512 Haggerty, S. E., & Baker, I. (1967, October). The alteration of olivine in basaltic
 513 and associated lavas. *Contrib. Mineral. Petrol.*, *16*(3), 233–257. doi: 10.1007/
 514 BF00371094
- 515 Koppers, A. A. P., Staudigel, H., & Wijbrans, J. R. (2000, May). Dating crys-
 516 talline groundmass separates of altered Cretaceous seamount basalts by the
 517 $^{40}\text{Ar}/^{39}\text{Ar}$ incremental heating technique. *Chem. Geol.*, *166*(1), 139–158. doi:
 518 10.1016/S0009-2541(99)00188-6
- 519 Krása, D., Heunemann, C., Leonhardt, R., & Petersen, N. (2003). Experimental
 520 procedure to detect multidomain remanence during Thellier–Thellier exper-
 521 iments. *Phys. Chem Earth (A/B/C)*, *28*(16), 681 - 687. (Paleo, Rock and
 522 Environmental Magnetism 2002) doi: 10.1016/S1474-7065(03)00122-0
- 523 Lawrence, K. P., Tauxe, L., Staudigel, H., Constable, C., Koppers, A., McIntosh,
 524 W. C., & Johnson, C. L. (2009). Paleomagnetic field properties near the
 525 southern hemisphere tangent cylinder. *Geochem. Geophys. Geosyst.*, *10*,
 526 Q01005. doi: doi:10.1029/2008GC002072
- 527 Levi, S. (1977, January). The effect of magnetite particle size on paleointensity de-
 528 terminations of the geomagnetic field. *Phys. Earth Planet. Inter.*, *13*(4), 245–
 529 259. doi: 10.1016/0031-9201(77)90107-8
- 530 Livermore, P. W., Fournier, A., Gallet, Y., & Bodin, T. (2018, December). Trans-
 531 dimensional inference of archeomagnetic intensity change. *Geophys. J. Int.*,
 532 *215*(3), 2008–2034. doi: 10.1093/gji/ggy383
- 533 Muxworthy, A. R. (2017). Considerations for latitudinal time-averaged-field
 534 palaeointensity analysis of the last five million years. *Front. Earth Sci.*, *0*.
 535 doi: 10.3389/feart.2017.00079
- 536 Nagata, T., Arai, Y., & Momose, K. (1963). Secular variation of the geomagnetic to-
 537 tal force during the last 5000 years. *J. Geophys. Res.*, *68*, 5277–5282.

- 538 Néel, L. (1949). Théorie du traînage magnétique des ferromagnétiques en grains fins
539 avec applications aux terres cuites. *Ann. géophys.*, *5*, 99–136.
- 540 Ozawa, A., Tagami, T., & Garcia, M. O. (2005, March). Unspiked K–Ar dating
541 of the Honolulu rejuvenated and Ko‘olau shield volcanism on O‘ahu, Hawai‘i.
542 *Earth Planet. Sci. Lett.*, *232*(1), 1–11. doi: 10.1016/j.epsl.2005.01.021
- 543 Paterson, G. A. (2011, October). A simple test for the presence of multidomain
544 behavior during paleointensity experiments. *J. Geophys. Res. Solid Earth*,
545 *116*(B10). doi: 10.1029/2011JB008369
- 546 Paterson, G. A., Tauxe, L., Biggin, A., Shaar, R., & Jonestrask, L. (2014). On im-
547 proving the selection of Thellier-type paleointensity data. *Geochemistry Geo-*
548 *physics Geosystems*, *15*(4). doi: 10.1002/2013GC005135
- 549 Pike, C., Roberts, A., & Verosub, K. (1999). Characterizing interactions in fine
550 magnetic particle systems using first order reversal curves. *J. Appl. Phys.*, *85*,
551 6660–6667.
- 552 Selkin, P., & Tauxe, L. (2000). Long-term variations in paleointensity. *Phil. Trans.*
553 *Roy. Soc. Lond.*, *358*, 1065–1088.
- 554 Shaar, R., Bechar, S., Finkelstein, I., Gallet, Y., Martine, M., Ebert, Y., ... Gonen,
555 L. (2020). Synchronizing archaeomagnetic field intensity records in the Levant
556 between the 23rd and 15th centuries BCE: chronological and methodological
557 implications. *Geochemistry Geophysics Geosystems*, *21*, e2020GC009251. doi:
558 10.1029/2020GC009251
- 559 Shcherbakov, V. P., Khokhlov, A. V., & Sycheva, N. K. (2019, January). Analysis
560 of the hypothesis of a Giant Gaussian Process as a means for describing sec-
561 ular variations of the geomagnetic field vector. *Izv. Phys. Solid Earth*, *55*(1),
562 182–194. doi: 10.1134/S1069351319010099
- 563 Sherrod, D. R., Nishimitsu, Y., & Tagami, T. (2003, June). New K–Ar ages and the
564 geologic evidence against rejuvenated-stage volcanism at Haleakala, East Maui,
565 a postshield-stage volcano of the Hawaiian island chain. *GSA Bulletin*, *115*(6),
566 683–694. doi: 10.1130/0016-7606(2003)115(0683:NKAATG)2.0.CO;2
- 567 Sherrod, D. R., Sinton, J. M., Watkins, S. E., & Brunt, K. M. (2007). Geologic map
568 of the State of Hawaii. *US geological survey open-file report*, *1089*, 83.
- 569 Tagami, T., Nishimitsu, Y., & Sherrod, D. R. (2003, February). Rejuvenated-
570 stage volcanism after 0.6-m.y. quiescence at West Maui volcano, Hawaii: New
571 evidence from K–Ar ages and chemistry of Lahaina Volcanics. *J. Volcanol.*
572 *Geotherm. Res.*, *120*(3), 207–214. doi: 10.1016/S0377-0273(02)00385-2
- 573 Tauxe, L. (2006). Long-term trends in paleointensity: The contribution of
574 DSDP/ODP submarine basaltic glass collections. *Physics of the Earth and*
575 *Planetary Interiors*, *156*(3–4), 223–241.
- 576 Tauxe, L., Asefaw, H., Behar, N., Koppers, A. A. P., & Shaar, R. (2022, August).
577 Paleointensity Estimates from the Pleistocene of Northern Israel: Implications
578 for hemispheric asymmetry in the time-averaged field. *Geochem. Geophys.*
579 *Geosyst.*, *n/a*(n/a), e2022GC010473. doi: 10.1029/2022GC010473
- 580 Tauxe, L., & Love, J. J. (2003, February). Paleointensity in Hawaiian Scien-
581 tific Drilling Project Hole (HSDP2): Results from submarine basaltic glass.
582 *Geochem. Geophys. Geosyst.*, *4*(2). doi: 10.1029/2001GC000276
- 583 Tauxe, L., Santos, C. N., Cych, B., Zhao, X., Roberts, A. P., Nagy, L., & Williams,
584 W. (2021, January). Understanding nonideal paleointensity recording in ig-
585 neous rocks: Insights from aging experiments on lava samples and the causes
586 and consequences of “fragile” curvature in Arai plots. *Geochem. Geophys.*
587 *Geosyst.*, *22*(1), e2020GC009423. doi: 10.1029/2020GC009423
- 588 Tauxe, L., & Staudigel, H. (2004, February). Strength of the geomagnetic field
589 in the Cretaceous Normal Superchron: New data from submarine basaltic
590 glass of the Troodos Ophiolite. *Geochem. Geophys. Geosyst.*, *5*(2). doi:
591 10.1029/2003GC000635
- 592 Wilson, R. L. (1970, April). Permanent aspects of the Earth’s non-dipole magnetic

- 593 field over Upper Tertiary times. *Geophys. J. Int.*, 19(4), 417–437. doi: 10
594 .1111/j.1365-246X.1970.tb06056.x
- 595 Yu, Y., Tauxe, L., & Genevey, A. (2004, February). Toward an optimal geomagnetic
596 field intensity determination technique. *Geochem. Geophys. Geosyst.*, 5(2). doi:
597 10.1029/2003GC000630
- 598 Zhao, X., Roberts, A. P., Heslop, D., Paterson, G. A., Li, Y., & Li, J. (2017, July).
599 Magnetic domain state diagnosis using hysteresis reversal curves. *J. Geophys.*
600 *Res. Solid Earth*, 122(7), 4767–4789. doi: 10.1002/2016JB013683
- 601 Ziegler, L., Constable, C., Johnson, C. L., & Tauxe, L. (2011). PADM2M: a pe-
602 nalized maximum likelihood model of the 0-2 Ma paleomagnetic axial dipole
603 moment. *Geophys. J. Int.*, 184, 1069-1089.
- 604 Zijderveld, J. D. A. (1967). *A.C. demagnetization of rocks: Analysis of results*.
605 Chapman and Hall.